

Supporting Information for

Bipolar electric-field switching of perpendicular magnetic tunnel junctions through voltage-controlled exchange coupling

Delin Zhang,^{1*} Mukund Bapna,^{2*} Wei Jiang,^{1*} Duarte Sousa,^{1*} Yu-Ching Liao,³ Zhengyang Zhao,¹ Yang Lv,¹ Protyush Sahu,¹ Deyuan Lyu,¹ Azad Naeemi,³ Tony Low,^{1†} Sara A Majetich,^{2†}
Jian-Ping Wang^{1†}

*These authors contributed equally to this work.

†Corresponding authors. Email: jpwang@umn.edu (J.P.W.), sara@cmu.edu (S.A.M.) and tlow@umn.edu (T.L.)

Supporting Information

MATERIALS AND METHODS

Sample preparation

The FePd SAF p-MTJ structures studied in this work were prepared on single crystal (001) MgO substrates by magnetron sputtering under an ultrahigh vacuum (base pressure $< 5.0 \times 10^{-8}$ Torr) under the same conditions as in our previous work (40). The FePd (3 nm)/Ru (1.1 nm)/FePd (3 nm) perpendicular SAF stack was prepared with a Cr (15 nm)/Pt (4 nm) seed layer, keeping the substrate temperature at 350 °C. The rest of the layers of the FePd SAF p-MTJ structures with a stack of Ta (0.8)/CFB (1.3)/MgO (2.0, 2.3)/CFB (1.3)/Ta (0.7)/[Pd (0.7)/Co (0.3)]₄/Pd (5)/capping layer (where the numbers in parentheses are thicknesses in nanometers) were grown after the substrate was cooled to room temperature. The 15-nm Pt capping layer was deposited for the conductive atomic force microscope (C-AFM) testing. Before device patterning, the FePd SAF p-MTJ stacks were annealed at 350 °C using rapid thermal annealing (RTA). Then the FePd SAF p-MTJ stacks were patterned into nano-pillars by e-beam lithography and Ar ion milling.

p-MTJ device testing

The spin transport properties were tested by using C-AFM at room temperature for 100-nm diameter FePd SAF p-MTJs. The C-AFM was an RHK UHV 350 with an R9 controller operating in contact mode. Si-doped AFM probe tips (Arrow-FM nanoworld) were made conducting by sputtering 200 nm of Pt onto a Ta adhesion layer (29). A Pt-coated AFM tip was used to make direct electrical contact with the top of FePd SAF p-MTJ pillars. In all the C-AFM measurements, the tip was grounded and V_{bias} (positive or negative) was applied at the bottom electrode. Thus, for a positive V_{bias} , the current flows from the bottom to the top, and for a negative V_{bias} , the current flows from the top to the bottom of FePd SAF p-MTJs. The E-field can

be calculated by dividing V_{bias} by the thickness of the MgO tunnel barrier. During the testing, a sweep rate of 150 Oe/sec was used to measure the R - H loops. A sweep rate of 500 mV/sec was used to measure the resistance versus bias voltage (R - V_{bias}) loops. For resistance versus time (R - t) traces, an acquisition rate of 1 MHz was used. A variable out-of-plane magnetic field with H_{ext} up to 1300 Oe was applied (29).

DFT calculation

The IEC of the SAF structure as a function of E-field was calculated using first-principles methods based on density functional theory (DFT). As implemented in the Vienna *ab initio* simulation package (VASP) code (41), the generalized gradient approximation (GGA) exchange-correlation potentials plus the projector augmented wave (PAW) method for the electron-ion interaction was used (42). Based on the experimental structure, we constructed a SAF structure with the stack of MgO (6)/Co₂Fe₆ (8)/Ta (6)/FePd (11), as shown in Fig. 3A in the main text, to study IEC between Co₂Fe₆ and FePd layers through a Ta spacer. The numbers indicate the atomic thickness for each layer, which corresponds to a thickness of 10.7, 8.5, 10.8, 15.7 Å for MgO, Co₂Fe₆, Ta, and FePd, respectively. This Co₂Fe₆ composition was used because it most closely reflects the stoichiometry after annealing the experimental sample to crystallize the MgO tunnel barrier (43). All self-consistent calculations were performed with a plane-wave cutoff of 400 eV. The geometric optimizations were carried out without any constraint until the force on each atom is less than 0.02 eV/Å and the change of total energy per cell is smaller than 10⁻⁴ eV. The Brillouin zone k-point sampling was set with a 9 × 9 × 1 Γ-centered Monkhorst-Pack grids. A vacuum layer thicker than 15 Å was applied along the z -direction to eliminate the interaction between slabs. The lattice constant and the atomic arrangement of the SAF structure were first relaxed without considering spin. The relaxed structure with a lattice constant of 2.92 Å was then

applied to study the magnetic interaction between the Co₂Fe₆ and FePd FM layers. Spin-orbit coupling effects were considered to study the magnetic anisotropy. The IEC was calculated by comparing the energy difference between FM and AFM couplings aligned of Co₂Fe₆ and FePd layers. An electric field is applied along the *z*-direction with the dipole corrections performed to avoid interactions between the periodically repeated images.

Section S1. Evaluation of H_C , $K_{u,\text{eff}}$, and ζ_{VCMA}

To quantitatively evaluate the E-field effect, the mean coercivity (H_C), effective magnetic anisotropy ($K_{u,\text{eff}}$), and VCMA coefficient (ζ_{VCMA}) of the FePd p-SAF free layer were obtained by measuring their minor *R-H* loops and fitting the switching field distribution (SFD) (29). To obtain SFD, multiple *R-H* loops were measured at a given V_{bias} . The H_C value was obtained by fitting SFD using the Kurkijärvi-Fulton-Dunkelberger equation:

$$\sigma = \left\{ \frac{1}{\tau_0 v} \exp \left[-K_{\text{eff}} V \left(1 - \frac{H M_s}{2K_{\text{eff}}} \right)^2 \right] \right\} \times \exp \left\{ - \int_0^H \frac{1}{\tau_0 v} \exp \left[\frac{-K_{\text{eff}} V}{k_B T} \left(1 - \frac{h M_s}{2K_{\text{eff}}} \right)^2 \right] dh \right\}. \quad (\text{S1})$$

where $\tau_0 \sim 10^{-9}$ second is the attempt time, $v \sim 350$ Oe/s is the ramping rate of H_{ext} , $M_s \sim 970$ emu/cm³ is the saturation magnetization of the FePd SAF free layer, k_B is the Boltzmann constant, and $T = 300$ K is the testing temperature. By fitting SFD from these minor *R-H* loops as shown in Fig. S4A, we obtained H_C , and $K_{u,\text{eff}}$ (ζ_{VCMA}), as plotted in Fig. S4C and S4D. H_C exhibits a typical linear behavior (9,18) and dramatically increases from ~ 145 Oe to ~ 900 Oe when V_{bias} sweeps from -0.75 V to +0.75 V. This is more than one order of magnitude larger than that of CoFeB/MgO/CoFeB p-MTJs, where H_C changes from 205 Oe to 290 Oe (14,29). The large H_C variation is attributed to the PMA modification of the CoFeB layer as well as the

modulation of the IEC strength between the FePd and CoFeB layers via the application of E-field.

Section S2. Evaluation of STT

To evaluate the contribution of the STT effect in our VCEC p-MTJs, we calculated the effective STT field (H_{STT}), in terms of the scalar functions given with Eqs. (S2 and S3) (44,45)

$$g(\theta) = \left[-4 + \frac{(1+\eta)^3(3+\cos\theta)}{4\eta^{3/2}} \right]^{-1} \quad (\text{S2})$$

$$H_{\text{STT}} = \frac{2\mu_B J g(\theta) \sin\theta}{\gamma e t_{\text{free}} M_s} \quad (\text{S3})$$

Here $\mu_B = 9.27 \times 10^{-24}$ A.m², $J_c = 1.1 \times 10^9$ A/m², $t_{\text{free}} = 1.3 \times 10^{-9}$ m, $e = 1.6 \times 10^{-19}$ A.s, $\gamma = 4\pi \times 1.6 \times 10^4$ m/A.s, $\eta = 0.65$, and $M_s = 8.9 \times 10^5$ A/m are the Bohr magneton, the switching current density, the thickness of the free layer, electron charge, gyromagnetic ratio, spin polarization, and saturation magnetization, respectively. θ is the angle between the free layer and the reference layer magnetization direction. The switching current density (J_c), the thickness of the free layer (t_{free}), spin polarization (η), and saturation magnetization (M_s) are obtained from our experimental results. Figure S3 plots the calculated H_{STT} as a function of the θ values. We find that the H_{STT} first gradually increases and reaches its maximum value $H_{\text{STT}} \sim 5$ Oe when $\theta \sim 150$ degrees, then decreases with the increasing θ , matching the trend in the literature (46). The $H_{\text{STT}} \sim 5$ Oe indicates that the STT effect is negligible in our experiment.

Section S3. Modeling the voltage-controlled interlayer exchange coupling (IEC)

We modeled the voltage dependence of the IEC within Bruno's theory in the context of the effective mass approximation (38). The model system is sketched in Fig. 4A. The IEC between FM_1 and FM_2 describes the energetic preference for the FM or AFM coupling. The coupling strength is defined as $J_{\text{ex}} = (E_{\text{FM}} - E_{\text{AFM}}) / 2$, where E_{FM} (E_{AFM}) is the total energy of the system per unit area for FM (AFM) configurations, and using Bruno's formula Eq. (1) in the main text. $J_{\text{ex}} > 0$ and $J_{\text{ex}} < 0$ represent the AFM and FM couplings, respectively. The FM_1 and FM_2 layers are magnetically coupled via itinerant electrons in the NM layer through spin-dependent reflections at the $\text{FM}_{(1,2)}/\text{NM}$ interfaces.

In our simulations, the FM layers with finite thicknesses were treated as Fabry-Perot cavities with multiple reflections within, which generates extra contributions to the total net reflection at the FM_2/NM and NM/FM_1 interfaces. As described in the main text, the reflection coefficients at the MgO/FM_2 , FM_2/NM and NM/FM_1 interfaces were defined as $r_{\text{A}}^{\uparrow(\downarrow)}$, $r_{\text{B}}^{\uparrow(\downarrow)}$, and $r_{\text{C}}^{\uparrow(\downarrow)}$ for spin-up and spin-down electrons, respectively. Since the FM_2 layer was surrounded by the different materials (the MgO tunnel barrier above and the NM layer below), we expected $r_{\text{A}}^{\uparrow(\downarrow)} \neq r_{\text{B}}^{\uparrow(\downarrow)}$ such that the FM_2 layer acts as an asymmetric Fabry-Perot cavity, where the net reflection coefficient that enters in Bruno's expression is

$$r_{\text{B}(\text{net})}^{\uparrow(\downarrow)} = \frac{r_{\text{B}\infty}^{\uparrow(\downarrow)} + r_{\text{A}}^{\uparrow(\downarrow)} e^{2ik_{\text{B}}^{\uparrow(\downarrow)}t_{\text{B}}}}{1 + r_{\text{B}\infty}^{\uparrow(\downarrow)} r_{\text{A}}^{\uparrow(\downarrow)} e^{2ik_{\text{B}}^{\uparrow(\downarrow)}t_{\text{B}}}} \quad (\text{S4})$$

Here t_{B} is the thickness of the FM_2 layer and $r_{\text{B}\infty}^{\uparrow(\downarrow)} = (k_{\text{F}} - k_{\text{B}}^{\uparrow(\downarrow)}) / (k_{\text{F}} + k_{\text{B}}^{\uparrow(\downarrow)})$ is the reflection coefficient at the FM_2/NM interface if the corresponding FM layer is infinite. The wave vector inside the FM_2 layer, $r_{\text{B}}^{\uparrow(\downarrow)}$, is related to the Fermi wave vector of the NM layer, k_{F} , via conservation of energy

$$\frac{\hbar^2}{2m_{\text{B}}} k_{\text{B}}^{\uparrow(\downarrow),2} + U_{\text{B}}^{\uparrow(\downarrow)} = \frac{\hbar^2}{2m} k_{\text{F}}^2 + U_0 \quad (\text{S5})$$

where the effective masses of the FM₂ layer and NM layer are m_{B} and m respectively, and the exchange splitting inside the FM₂ layer is $J_{\text{ex,B}} = U_{\text{B}}^{\downarrow} - U_{\text{B}}^{\uparrow}$. An equivalent set of equations is also valid at NM/FM₁ interface, giving rise to the FM₁ thickness-dependence of IEC.

Equation (S4) resumes to the well-known reflection coefficient of the Fabry-Perot problem when reflections at the MgO/FM₂ and FM₂/NM interfaces are the same (symmetric cavity).

We consider that an applied E-field causes a linear voltage drop inside the MgO tunnel barrier, as shown in Fig. 4A (bottom panel). An E-field inside the MgO tunnel barrier is given by V_{bias} / d , where d is the thickness of the MgO tunnel barrier. The barrier height of the MgO tunnel barrier is defined as U_1 . The E-field inside of the MgO tunnel barrier changes the reflection coefficient at the MgO/FM₂ interface, leading to the voltage-dependent $J_{\text{ex}}(V_{\text{bias}})$ via $r_{\text{A}}^{\uparrow(\downarrow)}(V_{\text{bias}})$ in Eq. (S4) and modifying the reflection coefficient $r_{\text{B}}^{\uparrow(\downarrow)}$, which translates to a voltage dependence of the IEC between FM₂ and FM₁ layers. The reflection coefficient is computed exactly by solving the tunneling problem for a trapezoidal barrier. Finally, we obtain the voltage-dependent reflection coefficient $r_{\text{A}}^{\uparrow(\downarrow)}(V_{\text{bias}})$:

$$r_{\text{A}}^{\uparrow(\downarrow)}(V_{\text{bias}}) = \frac{[ik_{\text{B}}^{\uparrow(\downarrow)} Ai(z_0) - A'i(z_0)][ik_{\text{A}}^{\uparrow(\downarrow)} Bi(z_{\text{d}}) - B'i(z_{\text{d}})] - [ik_{\text{A}}^{\uparrow(\downarrow)} Ai(z_{\text{d}}) - A'i(z_{\text{d}})][ik_{\text{B}}^{\uparrow(\downarrow)} Bi(z_0) - B'i(z_0)]}{[ik_{\text{B}}^{\uparrow(\downarrow)} Ai(z_0) + A'i(z_0)][ik_{\text{A}}^{\uparrow(\downarrow)} Bi(z_{\text{d}}) - B'i(z_{\text{d}})] - [ik_{\text{A}}^{\uparrow(\downarrow)} Ai(z_{\text{d}}) - A'i(z_{\text{d}})][ik_{\text{B}}^{\uparrow(\downarrow)} Bi(z_0) + B'i(z_0)]} \quad (\text{S6})$$

with Airy functions (Ai and Bi) and corresponding derivatives (A' and B' , where the prime symbol stands for derivative with respect to x , and not z) evaluated at points $z_0 = z$ ($x = 0$) and $z_{\text{d}} = z$ ($x = d$), where

$$z(x) = \left(\frac{2md^2}{\hbar^2 V_{bias}} \right)^{\frac{1}{3}} \left(U_1 - E - \frac{V_{bias}}{d} x \right) \quad (S7)$$

Here,

$$\frac{\hbar^2}{2m_A} k_A^{\uparrow(\downarrow),2} + U_A^{\uparrow(\downarrow)} - V_{bias} = \frac{\hbar^2}{2m} k_F^2 + U_0 \quad (S8)$$

Equation (S8) shows the relation of $k_A^{\uparrow(\downarrow)}$ and k_F , where $J_{ex,A} = U_A^\downarrow - U_A^\uparrow$ is the exchange splitting of the semi-infinite FM_1 layer.

In our simulations, we considered the thicknesses of all the layers in the SAF configuration to be the same as in the experiments: $t_C = 3$ nm, $t_B = 1.3$ nm, $D = 0.8$ nm, and $d = 2$ nm. Also, $E_F = 4$ eV, $J_A = J_C = 1$ eV, $J_B = 1.93$ eV, $U_A = U_B = U_C = 1$ eV, with $U_0 = 0$ eV and $U_1 = 5.4$ eV. Here, $\Delta E = 2a^2 J_{ex}$, where $a = 2.92$ Å is the in-plane lattice constant of the SAF configuration obtained from our DFT simulations. We assumed an intrinsic build-in field in all the results. The net effect was to change the bias from 0 V to 0.786 V, as estimated from the DFT calculations.

Section S4. Performance benchmarking of spin memories.

For STT-MRAM, our simulated results are comparable with the experimental results (47) by employing the macrospin model (48). Ref. (47) is one of the most recent papers on STT-MRAM with sub-30 nm diameters and 3-ns switching speed and 100 μ A write current. For SOT-MRAM, the micromagnetic simulation tool OOMMF (49) was used and the results were validated by experiments (50). Ref. (50) is a recent paper that had shown low write current density ($\sim 5.4 \times 10^6$ A/cm²) and fast write speed with write pulse width as short as 2 ns. In the benchmarking simulations, 5-ns and 10-ns hypothetical magnetization switching times were chosen. These

values show the same magnitude as STT does and can be roughly calculated based on Bruno's model. To quantify the potential impact of this VCEC switched p-MTJ device, we employed a 1000×32 bit memory array and carry out the benchmarking simulation of VCEC-MRAM against its STT-MRAM and SOT-MRAM counterparts based on the parameters of a 15-nm CMOS technology node (51). In the benchmarking simulation, the parameters (e.g. switching current density, switching time) used for the STT and SOT simulations are from the literature. For the VCEC-MTJ, we chose our experimental switching current density and 5-ns and 10-ns hypothetical magnetization switching times which is realistic in the experiment. The benchmarking results show that VCEC-MRAM dissipates more than an order of magnitude lower energy per write operation compared to STT-MRAM, as plotted in Fig. S9A. VCEC-MRAM is 2X denser than SOT-MRAM if implemented at the 15-nm CMOS technology node, and it will be 5.5X denser if implemented at the 7-nm CMOS technology node, as shown in Fig. S9B. We believe that these results (52) could be beneficial for a new generation of spin memory and logic applications.

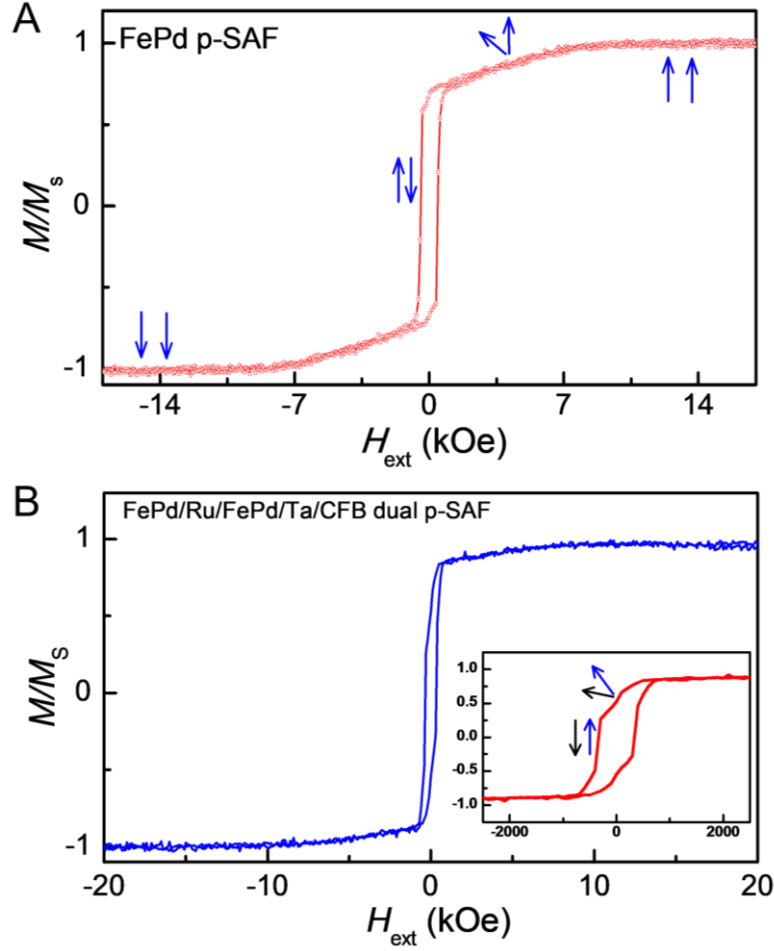


Fig. S1. Out-of-plane magnetic hysteresis (M - H) loops of FePd p-SAF structure. (A) The M - H loop of the FePd p-SAF structure with the stack of FePd (3.0 nm)/Ru (1.1 nm)/FePd (3.0 nm); **(B)** The M - H loop of the bottom SAF free layer by combining FePd SAF with a $\text{Co}_{20}\text{Fe}_{60}\text{B}_{20}$ layer. Spin-flop switching and spin-flip switching are observed at a high and low applied magnetic field, respectively.

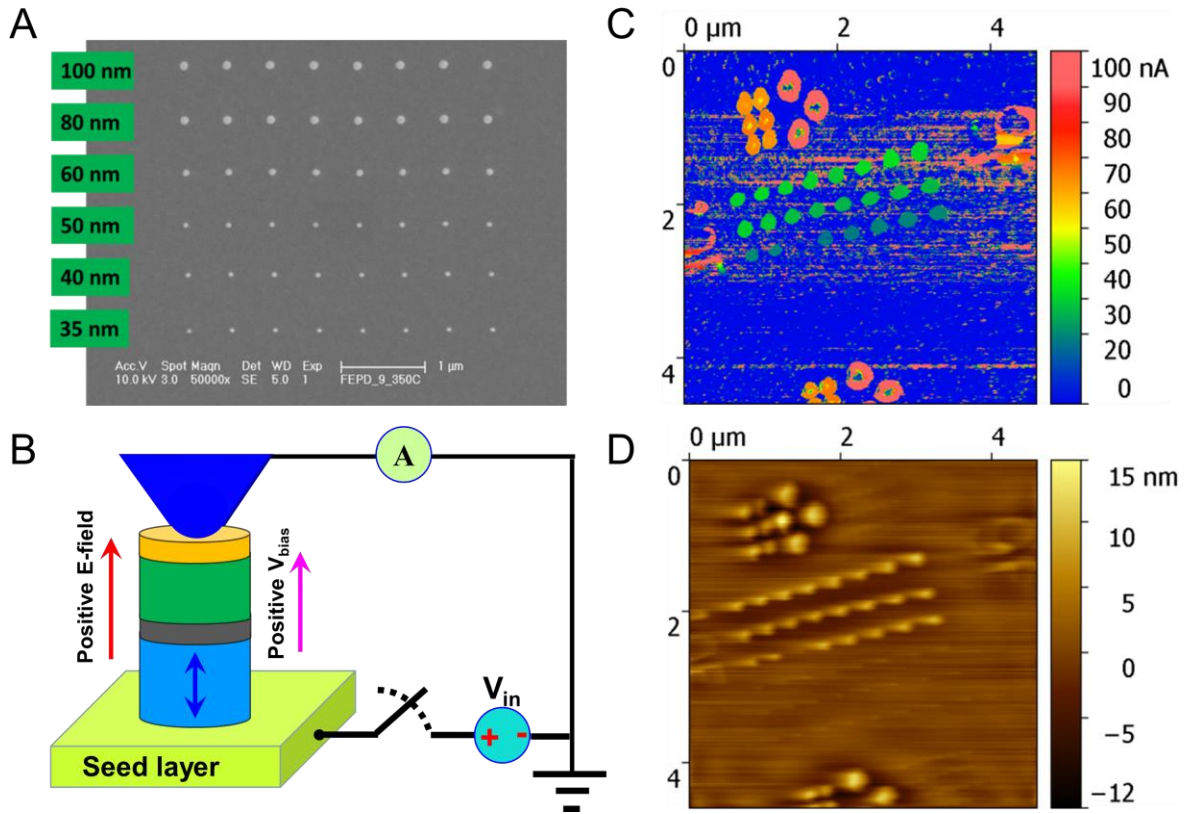


Fig. S2. Topographic images of nano-sized FePd SAF p-MTJ pillars. (A) SEM image of the top view of the patterned FePd SAF p-MTJ pillars with diameters of 35 nm ~ 250 nm. (B) the schematic of the C-AFM setup. In all the C-AFM measurements, the tip was grounded and V_{bias} (positive or negative) was applied at the bottom electrode. Thus, for a positive V_{bias} (positive E-field), the current flows from the bottom to the top of FePd SAF p-MTJs. (C) Topography measured by atomic force microscopy (AFM). (D) The current map measured by the conductive AFM (C-AFM) at 100 mV for the FePd SAF p-MTJ pillars.

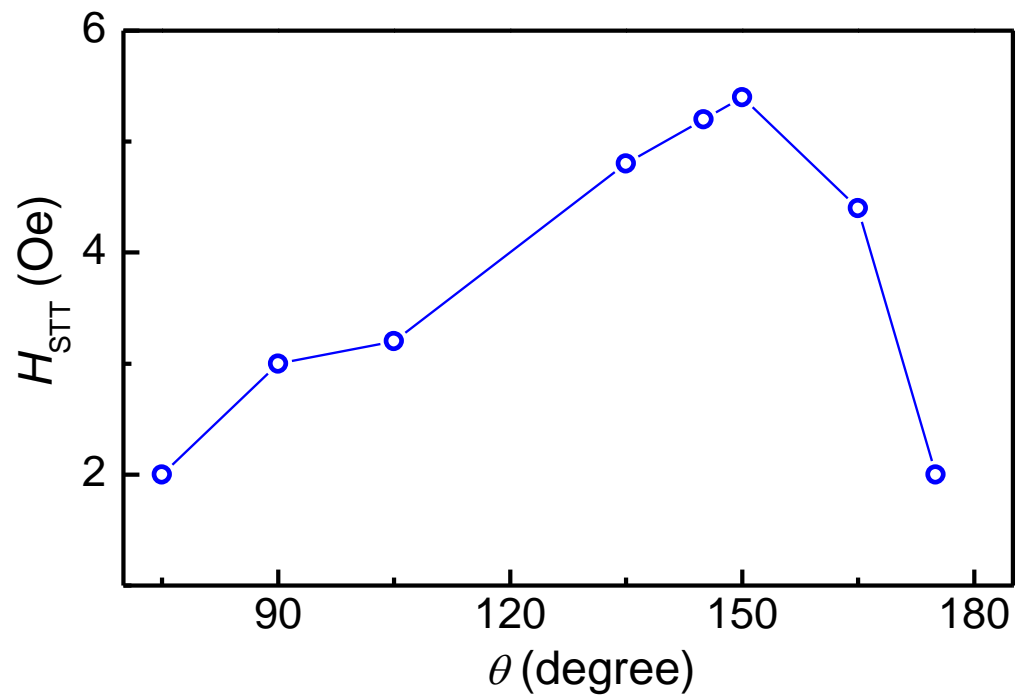


Fig. S3. STT effective field. The values of the effective STT field (H_{STT}) as a function of the θ values based on our experimental results.

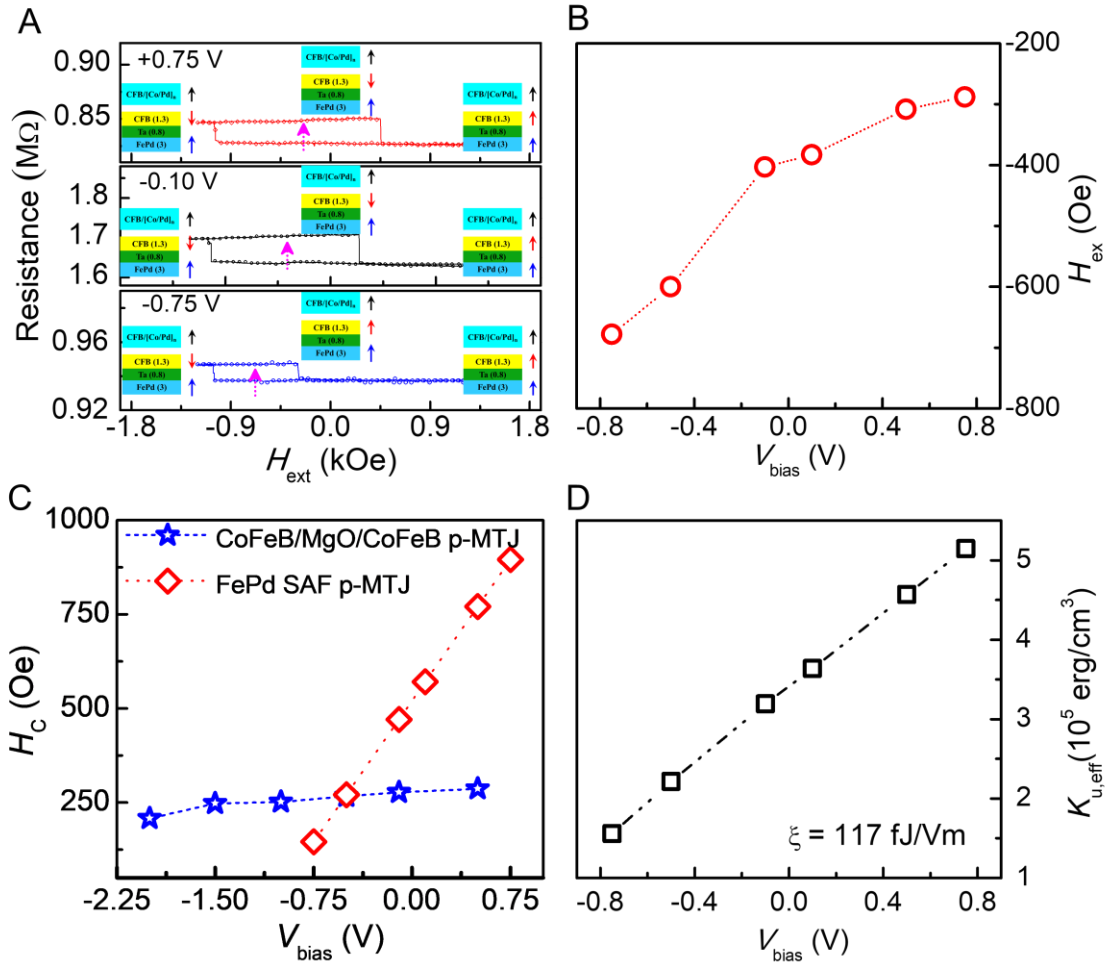


Fig. S4. E-field effect of FePd SAF p-MTJs. (A) The minor R - H loops of 100-nm FePd SAF p-MTJ devices with the different V_{bias} by varying H_{ext} from -1.3 kOe to +1.3 kOe. The center of each minor R - H loop is labeled with the arrow. Before sweeping H_{ext} , we applied a large H_{ext} to align the magnetization of the ferromagnetic layers. During the measurement of the R - H loops, the magnetization of the CoFeB layer is only switched by H_{ext} , as shown in the inset schematics of Fig. S4A. When $V_{bias}=-0.75$ V, the CoFeB and FePd layers prefer strong FM coupling, thus the CoFeB layer is switched under negative H_{ext} . When $V_{bias}=-0.1$ V and $+0.75$ V, the CoFeB and FePd layers prefer AFM coupling, thus the CoFeB layer is switched under positive H_{ext} . (B) The H_{ex} vs. V_{bias} curve, (C) The H_C vs. V_{bias} curve (red diamonds denotes FePd SAF MTJs; blue stars

presents CoFeB MTJs) and **(D)** $K_{u,\text{eff}}$ vs. V_{bias} for the 100-nm FePd SAF p-MTJ device. Here, the H_c and $K_{u,\text{eff}}$ values are obtained by fitting the switching field distribution (SFD) with the Kurkijärvi-Fulton-Dunkelberger equation. The ζ_{VCMA} for 100-nm FePd p-SAF p-MTJ devices was obtained from the linear fit.

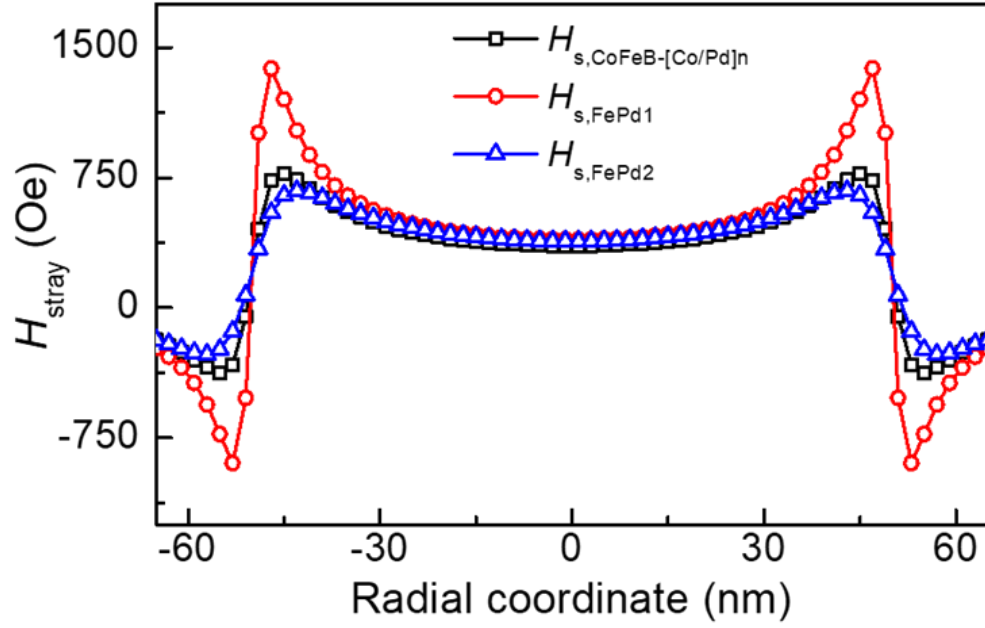


Fig. S5. Stray field effect. The calculated stray field (H_{stray}) of three ferromagnetic layers ($H_{\text{s,CoFeB-[Co/Pd]n}}$, $H_{\text{s,FePd1}}$, and $H_{\text{s,FePd2}}$). H_{stray} shown here is along z direction (perpendicular to the MTJ pillar plane). For the micromagnetic simulation, the thickness, magnetization of three layers are chosen from the experimental data.

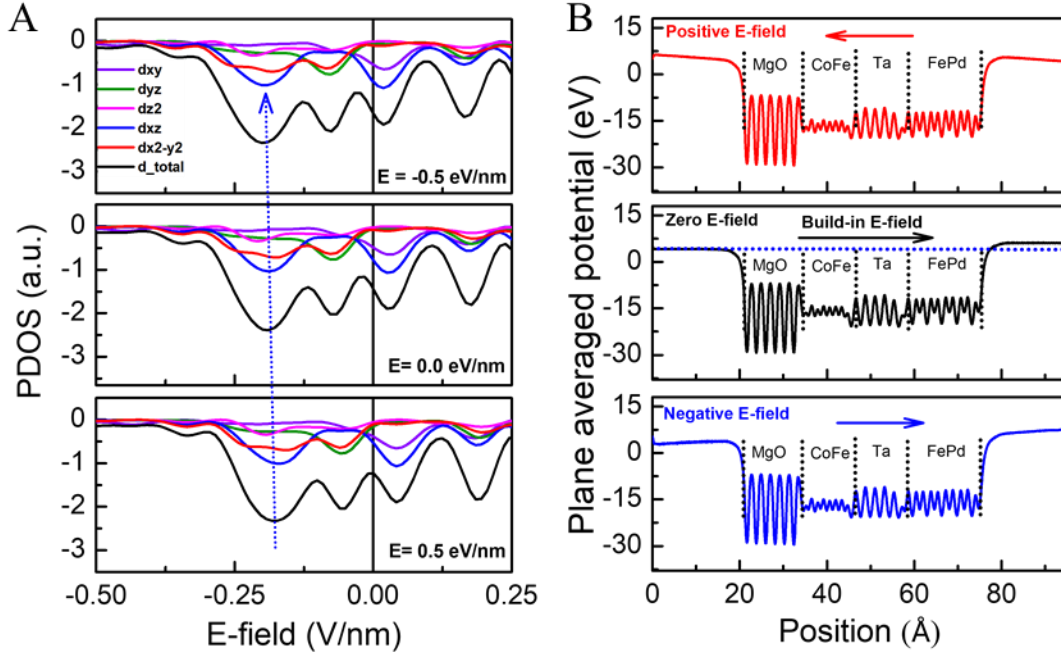


Fig. S6. The Fermi level shift and local potential profile under E-fields. (A) The projected density of states (PDOS) for interfacial Fe under different E-fields, which shows a clear Fermi level shift, indicating the electron accumulation and depletion at negative and positive E-Fields, respectively. (B) The local potential profiled for the system with positive, zero, and negative E-fields, where the positive E-field points upward (from bottom electrode to top electrode) and the negative E-field points downwards (from top electrode to bottom electrode). A built-in potential is induced due to the interaction at the interface between the MgO tunnel barrier and the CoFe layer.

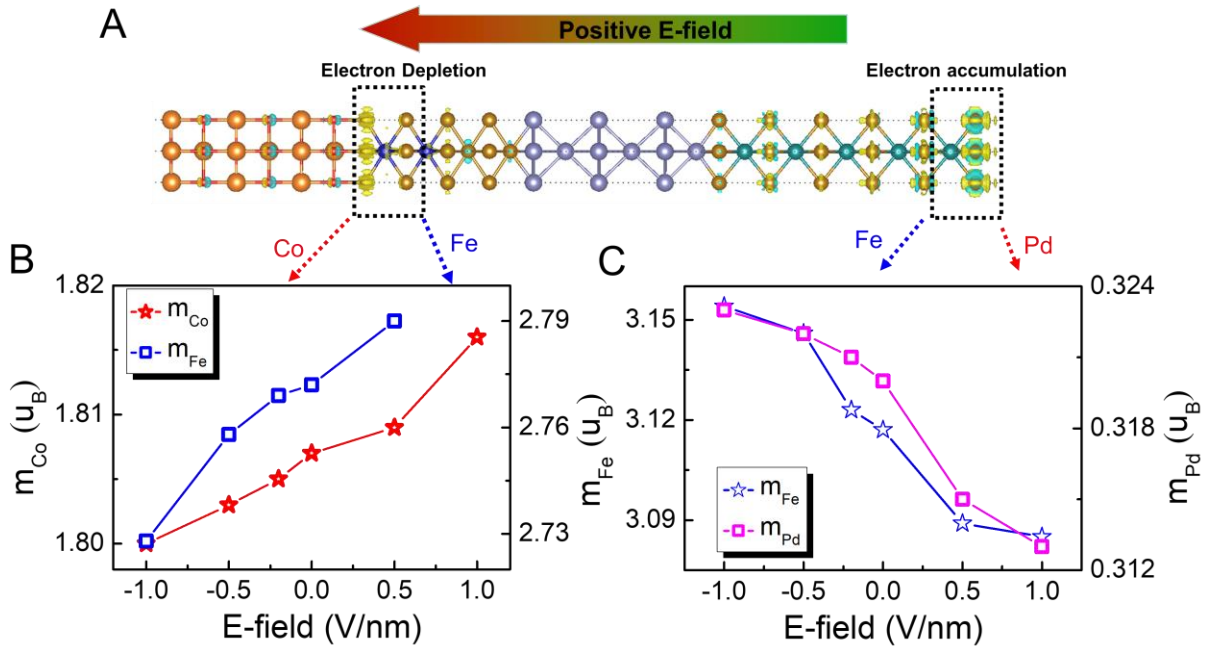


Fig. S7. VCMA effect at the interfaces. (A) The schematic of the optimized structural configuration used for first-principles calculations. Charge differential plot showing the electron depletion and accumulation at the MgO/CoFe and FePd/vacuum interface. (B) and (C) show the changes in the magnetic moment of interfacial CoFe and FePd as a function of E-field.

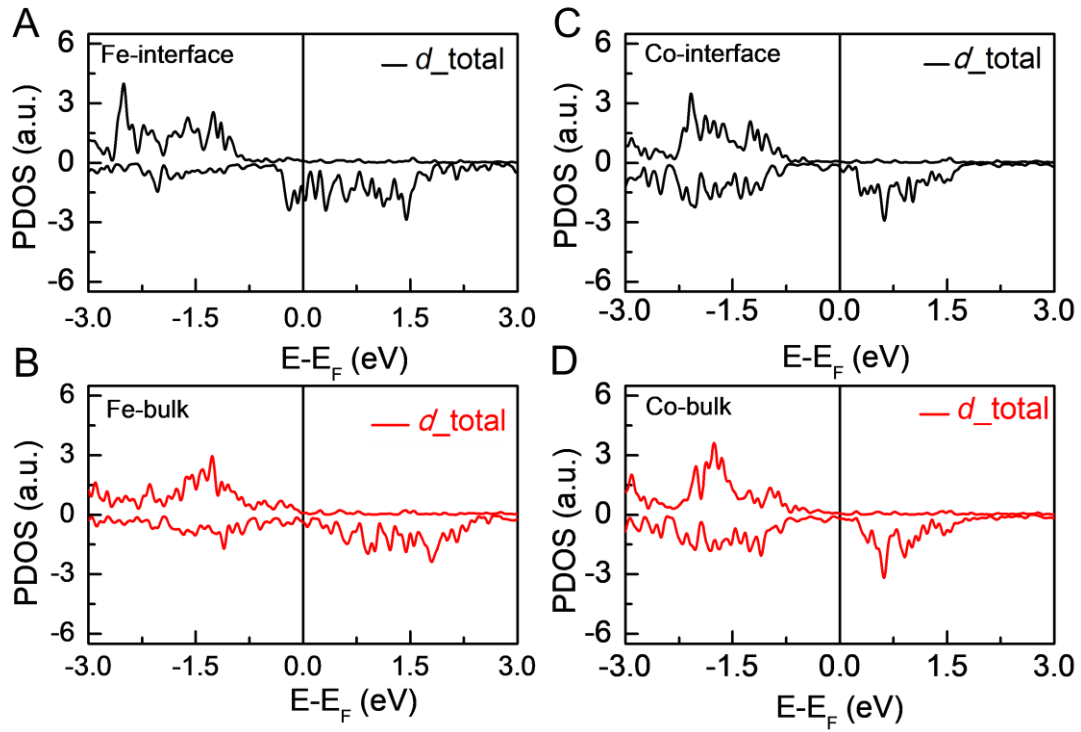


Fig. S8. Comparison of the interfacial and bulk electronic states. The projected density of states (PDOS) at the MgO/CoFe interface and in the bulk for the Fe atoms (**A**) and (**B**) and the Co atoms (**C**) and (**D**). The valence band electrons of *d*-orbitals at the interface clearly shift to the Fermi level compared with the bulk.

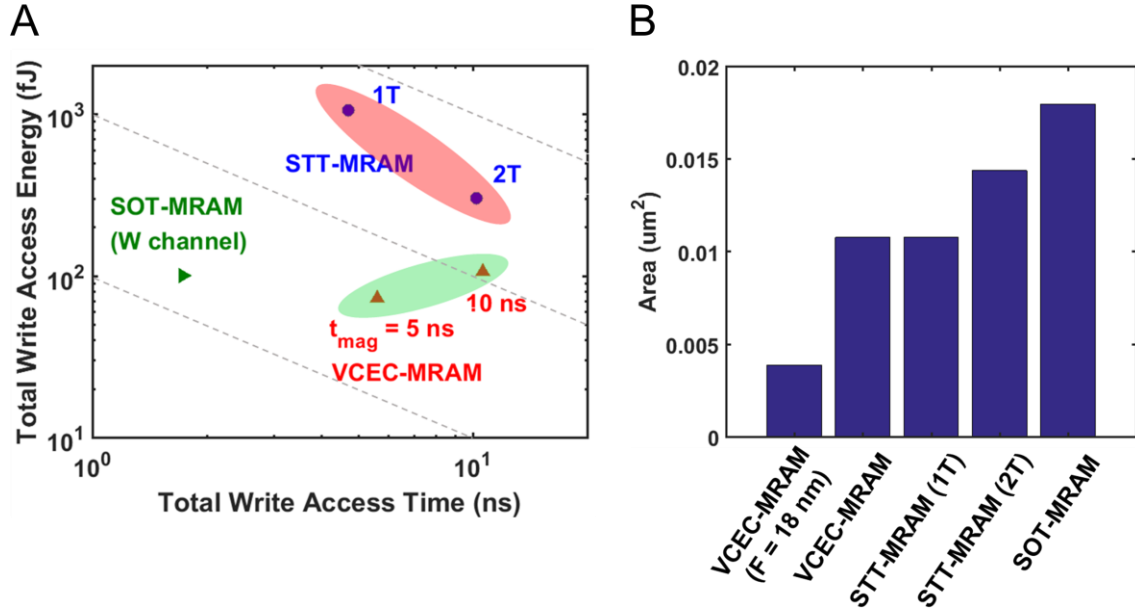


Fig. S9. Performance benchmarking of spin memories. (A) The write performance of the VCEC-MRAM compared to STT-MRAM and SOT-MRAM under a 1000×32 bit array. In our simulation, we used p-MTJ for STT-MRAM simulation, and in-plane MTJ for SOT-MRAM simulation. The magnetization switching time of VCEC-MTJ is hypothetically assumed to be 5 ns and 10 ns. (B) The comparison of the layout area for various spin memories including VCEC-MRAM, STT-MRAM, and SOT-MRAM. The half-metal pitch (F) of all the devices is 30 nm corresponding to the 15-nm CMOS technology node. For VCEC-MRAM, the case of F = 18 nm (corresponding to the 7-nm CMOS technology node) is also considered because of its scalability due to the high PMA and low write currents of the p-MTJ devices. For the STT-MRAM, the cases with one and two access transistors are considered.

REFERENCES

40. D. L. Zhang, C. Sun, Y. Lv, K. B. Schliep, Z. Zhao, J.-Y. Chen, P. M. Voyles, J.-P. Wang, L1₀-FePd synthetic antiferromagnet through a face-centered-cubic Ruthenium spacer utilized for perpendicular magnetic tunnel junctions. *Phys. Rev. Applied* 9, 044028 (2018).
41. G. Kresse, and J. Furthmüller, Efficiency of *ab-initio* total energy calculations for metals and semiconductors using a plane-wave basis set. *Comput. Mat. Sci.* 6, 15 (1996).
42. G. Kresse, and D. Joubert, From ultrasoft pseudopotentials to the projector augmented-wave method. *Phys. Rev. B* 59, 1758 (1999).
43. Z. Wang, M Saito, K. P. McKenna, S. Fukami, H. Sato, S. Ikeda, H. Ohno, Y. Ikuhara, Atomic-scale structure and local chemistry of CoFeB-MgO magnetic tunnel junctions. *Nano Lett.* 16, 1530-1536 (2016).
44. G. Finocchio, B. Azzerboni, G. D. Fuchs, R. A. Buhrman, L. Torres, Micromagnetic modeling of magnetization switching driven by spin-polarized current in magnetic tunnel junctions. *J. App. Phys.* 101, 063914 (2007).
45. G. Finocchio, M. Carpentieri, B. Azzerboni, L. Torres, E. Martinez, L. Lopez-Diaz, Micromagnetic simulations of nanosecond magnetization reversal processes in magnetic nanopillar. *J. Appl. Phys.* 99, 08G522 (2006).
46. J. C. Slonczewski, Current-driven excitation of magnetic multilayers. *J. Magn. Magn. Mater.* 159, L1-L7 (1996).
47. D. Saida, S. Kashiwada, M. Yakabe, T. Daibou, M. Fukumoto, S. Miwa, Y. Suzuki, K. Abe, H. Noguchi, J. Ito, S. Fujita, 1×-to 2×-nm perpendicular MTJ switching at sub-3-ns pulses below 100 μa for high-performance embedded STT-MRAM for Sub-20-nm CMOS. *IEEE Trans. Electron Devices* 64, 2, 427-431 (2017).
48. J. Z. Sun, Spin-current interaction with a monodomain magnetic body: A model study. *Phys. Rev. B* 62, 570-578 (2000).
49. M. J. Donahue, and D. G. Porter, OOMMF User's Guide, Version 1.0 Interagency Report NISTIR 6376, National Institute of Standards and Technology, Gaithersburg, MD (1999). <http://math.nist.gov/oommf/>.
50. S. Shi, Y. Ou, S. V. Aradhya, D. C. Ralph, R. A. Buhrman, Fast low-current spin-orbit-torque switching of magnetic tunnel junctions through atomic modifications of the free-layer interfaces. *Phys. Rev. Applied.* 9, 011002 (2018).
51. Y.-C. Liao, C. Pan, and A. Naeemi, Benchmarking and optimization of spintronic memory arrays. *IEEE J. Explor. Solid-State Computat. Devices Circuits (JxCDC)* 6, 9 (2020).
52. D. Zhang, M. Bapna, W. Jiang, D. P. de Sousa, Y.-C. Liao, Z. Zhao, Y. Lv, P. Sahu, D. Lyu, A. Naeemi, T. Low, S. A. Majetich, and J.-P. Wang, Bipolar electric field switching of perpendicular magnetic tunnel junctions through voltage controlled exchange coupling. arXiv preprint arXiv:1912.10289, 2019.